Eng. Sci., 2021, **17**, 231–241

Engineered Science

DOI: https://dx.doi.org/10.30919/es8d595

Heterostructure Necklace-like NiO-$NiCo_2O_4$ Hybrid with Superior Catalytic Capability as Electrocatalyst for Li-Oxygen Batteries

Zeinab Mohamed,[1, 2] Guoliang Zhang,[2] Biao He[3,*] and Yuqi Fan[1,*]

Abstract

The advancement of the Li-O_2 battery is still in its beginning stages. Heterostructure composites, especially transition-metal oxide-based materials, were proven as efficient electrocatalysts which can significantly improve the sluggish reaction efficiency and battery performance. This research aimed to synthesize and investigate the bi-functional NiO-$NiCo_2O_4$ microspheres as a cathode in aprotic Li-O_2 batteries for boosting electrochemical efficiency utilizing a simple hydrothermal method and annealing. Based on the existing electrochemical features of NiO-$NiCo_2O_4$ catalysts, the unique hybrid structure and dynamical impact between the nickel cobaltite and nickel oxide phases may support and promote electro-catalysis. $NiCo_2O_4$ helps enhance oxygen reduction and evolution reactions at the positive electrode, as well as NiO probably promotes the degradation of some by-products. In addition, the unique necklace-like morphology leads to continuing oxygen flowing, storing the discharge products, and boosting the transportation of ions and electrons. A substantial capacity of 23163/20770 mAh g^{-1} was achieved, and the overpotential of 0.13/0.61 V was minimized in discharge/charge. Moreover, the positive electrode can hold the cycle more than 170 times without any apparent variation at a current of 200 mA g^{-1}, indicating that the as-synthesized necklace-like hetero structure NiO-$NiCo_2O_4$ is an interesting driving force cathode catalyzer for Li-O_2 batteries.

Keywords: Li-O_2 battery; Transition metal oxide; Heterostructure; NiO-$NiCo_2O_4$ microspheres.
Received: 17 September 2021; Revised: 08 December 2021; Accepted: 08 December 2021.
Article type: Research article.

1. Introduction

The rising demand for future energy storage systems has resulted in rapidly growing research on rechargeable batteries as well-qualified applicant energy storage devices for the coming generation. Li-O_2 battery has recently acquired a lot of interest, attributed to their excessive theoretical energy density (11140 KW kg^{-1}), which is substantial compared to gasoline.[1,2] In addition, mobility, portable devices, and grid energy storage are all possible and promising applications. A further important feature of Li-O_2 batteries is that they do not require cathode reactants to be stored within the batteries. Because the reactant is oxygen, and oxygen can be header and footer tools resupplied at any time; as a result, batteries can be made lighter and more suitable for portable devices. The Li-O_2 battery hybridizes a lithium battery and a fuel cell, using lithium-ion and oxygen-based technology. A lithium foil anode and electrolyte provide lithium-ion channels between the negative and the positive electrodes in a standard Li-O_2 battery. Electrons use the external circuit to perform electrical work during the discharge process, while lithium ions travel to the positive electrode; conversely, oxygen is released into the positive electrode when the lithium metal sheets are charged to the anode.[2-5]

The discharge and charge processes in the Li-O_2 battery are associated respectively with the oxygen reduction reaction (ORR) and the oxygen evolution reaction (OER). The advancement of the Li-O_2 battery is still in its beginning stages, with numerous challenges and issues to overcome before commercialization. Cyclability and round-trip efficiency, both dependent on the reaction mechanisms of the reduction and

[1] *Institute of Environment and Ecology, Shandong Normal University, Jinan, 250014, China.*
[2] *Key Laboratory for Liquid-Solid Structural Evolution and Processing of Materials (Ministry of Education), Shandong University, 17923 Jingshi Road, Jinan 250061, China.*
[3] *Institute for Materials, Ruhr-Universität Bochum, Universitätsstr. 150, 44803 Bochum, Germany.*
**E-mail:* yuqifan@sdnu.edu.cn (Y. Fan); biao.he@rub.de (H. Biao)

evolution of the oxygen at the cathode, are two of the most severe issues limiting Li-O_2 battery effectiveness.[5,6] One key to achieving high-performance Li-O_2 batteries is developing a dual-function electrical catalyst to effectively boost both ORR and OER. Several substances as cathode materials have already been explored, such as carbonaceous-based cathodes[7-9] noble metal and metal oxides,[10,11] perovskite catalysts,[12] redox mediator.[13,14] However, the optimal cathode consists of a low-cost, lightweight, durable, and porous material with a wide surface area to enable the rapid decomposition of lithium oxides to improve Li-O_2 battery capacity, round trip efficiency, and charge stability. Transition metal oxides are more suited for possible application owing to their high electrical and catalytic activity, reduced cost, and large reserves of expensive noble metals. For instance, many Co or Ni-based oxide structures have been reported, including $FeCo_2O_4$ porous nanorods and $CuCo_2O_4$ nanoparticles as effective Li-O_2 and Li-air catalysts.[15,16] He *et al*. constructed a modified cubic spinel of NiFeO with 3D architecture, developing a high-rate reliable electrocatalyst for Li-O_2 batteries using a super assembly method. At a high current of 1000 mA g^{-1}, a massive specific capacity of 23413 $mAhg^{-1}$ and exceptionally 193 cycles are achieved, and 300 cycles with a current of 500 mA g^{-1}.[17]

For energy storage applications, nanocrystals with heterostructures and various oxidation states are particularly future-oriented because of their tunable electronic characteristics and optimized interfacial catalysis. The interface effect and the existence of the internal electrical field allow it to increase surface dynamics and encourage charging transport. Thus, the features and construction of heterostructure compounds using two distinct substances could increase the electrical efficiency and the ion diffusion capability of Li-O_2 batteries. In the dissociation of by-products containing carbonate/carboxylate species, hexagonal NiO was expected to play a crucial role, benefiting the valid formation/decomposition of Li_2O_2 products.[18] However, pure NiO shows inferior electroactivity since it binds oxygen too weak due to its unfavorable electron configuration, which inhibits the adsorption of the oxygen-containing intermediates.[18,19] On the other hand, the existing review has shown that $NiCo_2O_4$ has outstanding electrocatalytic behavior and electrical properties that are always greater than the counter single metallic oxides (NiO and Co_3O_4).[19] The octahedral sites in $NiCo_2O_4$ are occupied by divalent nickel ions, while the trivalent cobalt ions are distributed between octahedral and tetrahedral sites, and the abundantly active catalytic sites from two reducing-oxidation pairs derived nickel cobaltite to be considered one of the most promising bi-function catalysts.[20-22] Zhang *et al.* designed a conductive noncarbon and binder-free cathode using CeO_2 NPs patterned on $NiCo_2O_4$ nanowire array (NWAs) grown on carbon cloth (CCs). The Li-O_2 battery showed significantly lower overpotentials, a higher discharge capacity, and improved cycle performance.[23] Dong *et al.* presented a Pt/NiO composite with excellent catalytic activity as an electrode for Li-O_2 batteries, allowing for substantially increased capacity utilization, good cycling stability, a high initial capacity of 2329 mAh g^{-1}, and no noticeable voltage decrease during cycling.[24]

Therefore, benefiting from the above-mentioned characteristics of nickel cobaltite and nickel oxide, we proposed to produce a heterostructure NiO-$NiCo_2O_4$ microsphere and change the annealing temperature to vary the electronic structure of $NiCo_2O_4$ cubic spinel. The study found that the heterogeneous NiO-$NiCo_2O_4$ structures possess ultrahigh catalytic activity and excellent electrochemical performance as a consequence of the surface containing various metal cations with paramount octahedral coordination. The porous heterostructure with ample interfaces enables catalysts to expose more active sites, while the highly active redox Ni^{2+}/Ni^{3+} and Co^{2+}/Co^{3+} species might be significant in influencing discharge products to evolve in constant current charge-discharge cycles. The results show that the well-designed NiO-$NiCo_2O_4$ catalyst has an exceptionally high specific capacity, stable cycle capacity, and good rate performance. This article provided an interesting direction and insight for the fabrication of Li-O_2 batteries with highly-output heterostructure mixed metal oxide electrocatalysts.

2. Experimental method and instrumentation

2.1 Catalyst Preparation

All the reagents were analytical grade and do not need to be purified further. NiO-$NiCo_2O_4$ microspheres were synthesized according to a typical hydrothermal preparation method, and their synthetic schematic and morphological changes were shown in Fig. 1. First, 2 mmol of $NiCl_2 \cdot 6H_2O$ and 4 mmol of $CoCl_2 \cdot 6H_2O$ were dissolved in 30 ml ethylene glycol (EG) with continuous stirring, followed by slow addition of 2.9 g sodium acetate (NaAc), it continued mixing for an hour. Then converted into a lined Teflon stainless-steel autoclave, maintained at 200 °C, and remained in an oven for 20 hours. The resultant product was washed multiple times with ethanol and dried under vacuum at 60 °C overnight after cooling down to the ambient temperature. Finally, for two hours, in a tube furnace, the dried product was annealed to a heating rate of 2 °C min^{-1} under atmospheric air to achieve the desired products. Calcination temperatures of 400, 500, 600, and 700 °C were employed to form $NiCO_2O_4$ microspheres designated NCO-400, NCO-500, NCO-600, and NCO-700.

2.2 Positive electrode preparation

The positive electrode was constructed utilizing the as-synthesized cathode catalyzers to examine their electrochemical efficiency in Li-O_2 batteries. In a typical procedure, a slurry mixture was formed by ultrasonic sonicating a solution of 3 mL isopropanol for 20 minutes with a specified amount of the produced catalysts, Ketjen Black (KB), and poly (tetrafluoroethylene) (PTFE) as a binder (in 4:4:2 mass ratio). The mixture was sprayed evenly on the

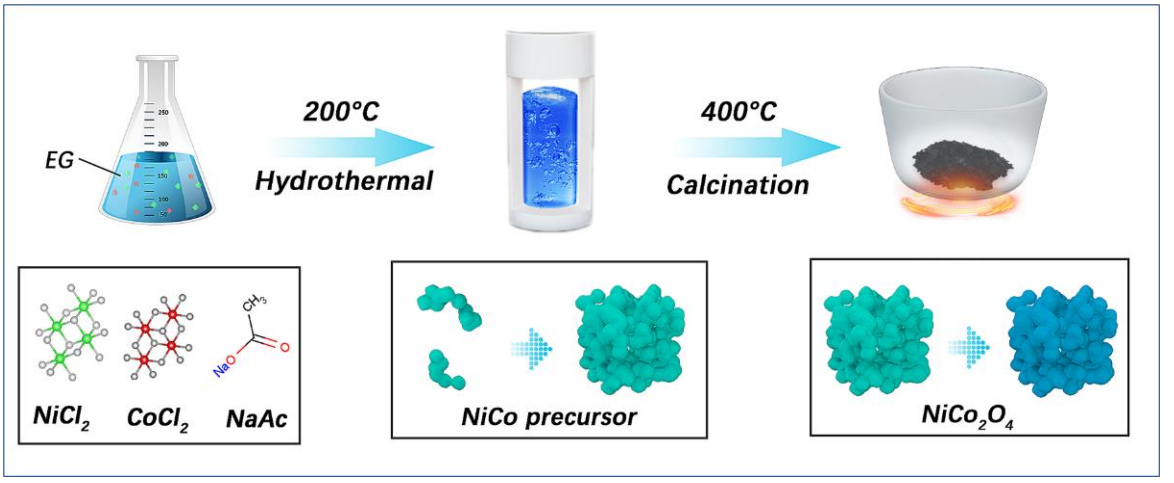

Fig. 1 Schematic illustration of the as-prepared heterostructure NCO microspheres.

nummular carbon paper and dried for ten hours at 120 °C in a vacuum oven.

2.3 Li-O_2 battery assembly

A formulated positive electrode (oxygen electrode), a fiberglass separator, a lithium metal foil as a negative electrode (anode), and an electrolyte of 1 M $LiNO_3$/DMSO make up a Li-O_2 cell. All cells are built in a glove box filled with argon at room temperature (H_2O 0.1 ppm, O_2 0.1 ppm). The Li-O_2 batteries were brought out of the argon-filled glove box and placed in a gastight bottle containing ultra-high quality oxygen gas. Before testing, the batteries were given a 5-hour rest under oxygen. All charge/discharge and electrochemical experiments were conducted at a constant temperature of 25 °C.

2.4 Characterization

The examination of the microstructure of the as-prepared NCO catalysts was carried out through a scanning electron microscope (SU-70) coupled with an energy-dispersive X-ray spectrometer (EDS). The crystal structure of the NCO materials is characterized using XRD (Rigaku D/Max-r B, Cu-Kα, 40kV, current of 40mA, and angle range of 10-70° at 4° min^{-1}). Raman spectra were conducted using (the inVia model Raman spectrometer from Renishaw, 785 nm, and 100-2000 cm^{-1}). The chemical states of the elements were confirmed using a thermal fisher Scientific slab 250 X-Ray photoelectron spectrometer (XPS). The Material's specific surface area and pore size distribution were determined using the Brunauer-Emmett Teller method (BET) utilizing a micrometric analyzer (ap2020), at 77 k, under N_2. Linear sweep cyclic voltammetry (CV) was utilized to understand the electrode's electrochemical reaction mechanisms and determine the catalyzation efficiency of the as-prepared samples. The scan rate is set to 0.1 mv s^{-1} and the scan voltage range is 2.35-4.35 V. In this work, the ct-2001a blue battery system of Wuhan blue battery electronic for consistency was employed, and the mass of active components in the cathode was used to standardize the capacity of Li-O_2 batteries and is denoted by mAh g^{-1}. In this work, we performed the galvanostatic charge/discharge cycling at a current density of 200 mA g^{-1} and cutoff capacities of 600 and 1000 mAh g^{-1}. The charge and discharge voltage are set between 2.35 and 4.35 V. At the specified primary regions, the ex-situ high-resolution XPS from Li 1s was performed after the first cycle discharge at the current density of 200 mA g^{-1} and a capacity limitation of 1000 mAh g^{-1}.

3. Results and discussion

The hydrothermal approach was used to produce NiO-$NiCo_2O_4$ microspheres featuring a heterostructure, as illustrated in Fig. 1. The necklace-like $NiCo_2O_4$ microspheres synthesizing method can be explained: dehydration processes were carried out from ethylene glycol (EG), and water (H_2O) was generated in a sealed autoclave with high temperature and pressure during the hydrothermal reaction. The sodium acetate (NaAc) was hydrolyzed for alkaline conditions. Then, nickel and cobalt salt reacted with OH^- to the formation of nickel cobaltite. The product was washed and dried and further annealed under atmospheric air with different temperatures to achieve the desired materials. Calcination temperatures of 400, 500, 600, and 700 °C were employed to form heterostructure NiO-$NiCo_2O_4$ microspheres designated NCO-400, NCO-500, NCO-600, and NCO-700, respectively.

The morphology of the as-prepared catalysts was explored through the Scanning Electron Microscopy technique (SEM), as presented in Figs. 2(b, c). All the as-prepared NCO samples display the necklace-like shape formed of small spheres with different diameters and necklace lengths at different calcination temperatures. Noteworthily, the final products held the initial geometry and morphology of the precursor molecules after heat treatment, as shown in Fig. S1 (supporting information). The morphology of attained materials may result from the hydrothermal preparation method utilized. A typical $NiCo_2O_4$ spinel needle-like shape was reported by Devaguptapu *et al.*[25] These needles consist of numerous nanoparticles with a greater tendency to agglomerate due to magnetic interactions among the particles

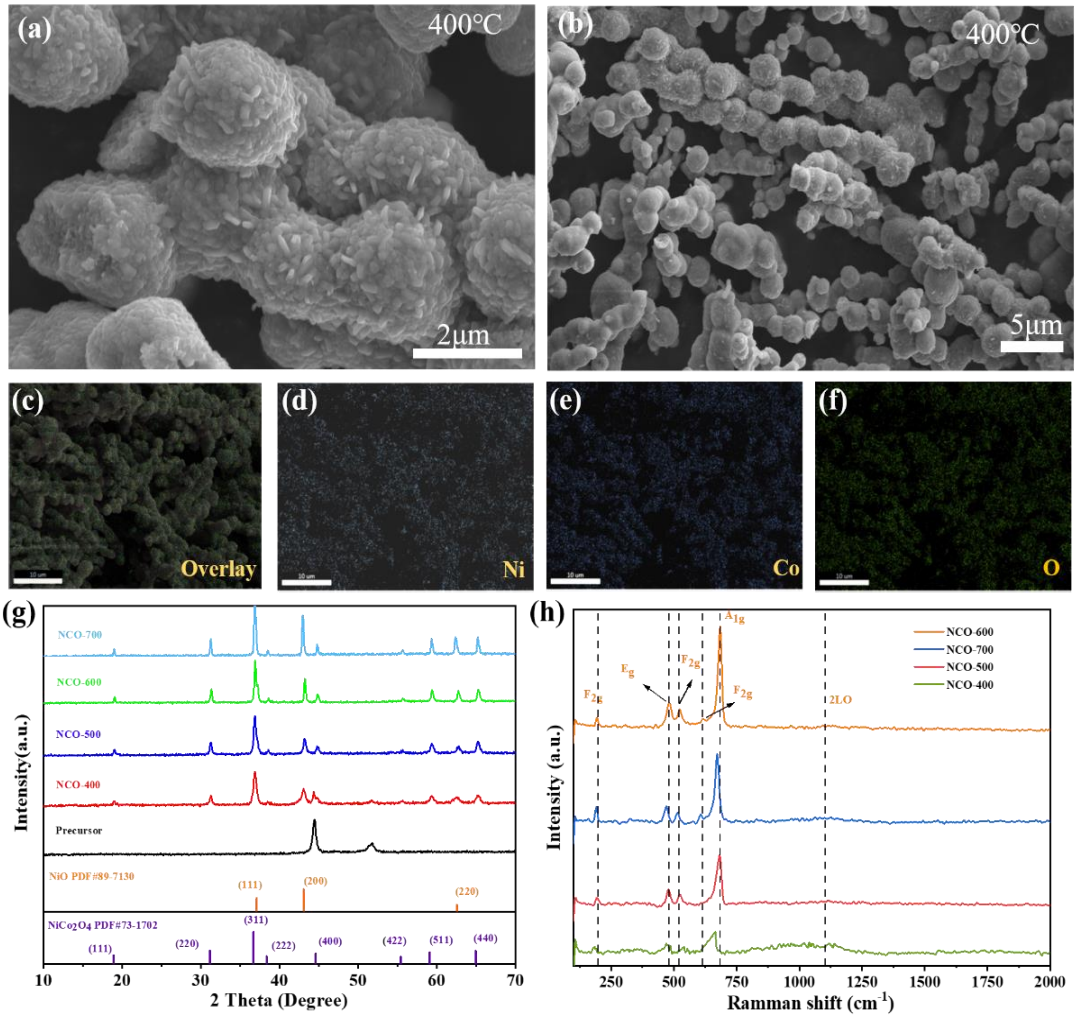

Fig. 2 (a, b) SEM photos of the NCO-400 sample with different magnification; (c-f) Energy-dispersive X-ray spectroscopy (EDS) mapping of the NCO-400; (g) The XRD graph of the obtained NCO microsphere samples at different calcinating temperatures; (h) Raman profiles of the as-synthesized NCO samples at different calcination temperatures.

than our synthesized samples. Qin *et al.*[26] obtained urchin-like composed $NiCo_2O_4$, in which samples have spheres composed of nanowires in inverse configuration. Both morphologies have been reported many times. In our situation, the necklace-like architectures are isolated. However, they are not as slender as wires and needles; the necklaces are more like branches formed of several different size spheres. The elemental mapping analysis shown in Figs. 2(c-f) displays the distribution of Ni, Co, and O elements on NCO, showing that these elementals cover evenly on the samples and further indicate a uniform oxide structure.

X-ray diffraction analysis (XRD) was carried out to identify the phase composition and the crystal structure of the as-prepared NiO-$NiCo_2O_4$ microspheres at different annealing temperatures. In Fig. 2(d), the XRD analysis of NCO catalysts revealed the exhibition of the cubic NiO phase along with the cubic $NiCo_2O_4$ spinel oxide under all calcination temperatures. The reflections are indexed properly to the NiO and $NiCo_2O_4$ cubic structures, as evidenced by $NiCo_2O_4$ JCPDS card No. 73-1702 and NiO No. 89-7130 references. Reflections at 2theta values of 18.9º, 31.2º, 36.7º, 38.4º, 44.6º, 55.4º, 59.1º, and 64.7º are corresponding to the (111), (220), (311), (222), (400), (422), (511) and (440) planes of $NiCo_2O_4$, respectively. The detection of the additional peaks at 2 thetas of 37.09º, 43.09º, and 62.58º values corresponding to (111), (200), and (220) planes related to NiO cubic, respectively, confirmed that the as-prepared catalysts composed of two phases NiO and $NiCo_2O_4$. The findings show that 400 °C is sufficient to produce crystalline NiO along with the $NiCo_2O_4$ spinel. The peak intensities of the cubic NiO increased as the temperature kept rising; this was in agreement that the spinel $NiCo_2O_4$ oxide decomposes to NiO at a temperature above 400 °C.[27] The absence of any unidentified peaks demonstrated the purity of the samples. The lattice constant and the crystallite size are summarized in Table S1 (Supporting information). They were calculated from the obtained XRD pattern by applying the Debye-Scherrer method.[28] The results show that the hydrothermal conditions, time, and temperature played a crucial role and led to the larger crystallite size. The calculations showed that as the annealing temperature rises, larger crystallite sizes were obtained. As can be seen in Table S1, the lattice parameter "a" of the NiO phase ranges from

4.192 to 4.203 Å. Since, the lattice parameter of a pure cubic NiO is 4.1944 Å (PDF#89-7130), while the value of $NiCo_2O_4$ phases varies between 8.071 to 8.083 Å (8.114 Å for pure $NiCo_2O_4$, PDF#73-1702), both phases have matched XRD patterns and the overlap of peaks obtains no reliable identification. The crystallite size grows for both phases as the calcination temperature rises; this is most likely owing to the spinel phase's faster decomposition rate, the partial decomposition of the spinel phase, resulting in NiO segregation, is well known to occur beyond 400 °C.[26-31]

Figure 2(e) shows the results achieved by Raman Spectroscopy. They illustrate the variations in the structure of the synthetic samples of vibrions and composition. The primary peaks of the spinal structural modes between 180 and 800 cm^{-1} in all samples are observed. A mode can be characterized in the dynamic system as the excitement of a standing wave. Each frequency characterizes one or a few frequencies to present a certain quantity of energy in every store. These patterns are marked as A, B, E, and L, which give a specific set of points vibrational movements. In samples annealed at 600 °C, the highest intensity of the peak is shown. With a temperature rise, the local maximum height lifts off. The vibrational peaks of the NCO-600 spectra were accurately 194, 482, 522, 619, and 685 cm^{-1}, respectively corresponding in the modes E_{2g}, E_g, F_{2g}, F_{2g}, and A_{1g} of $NiCo_2O_4$.[32] The A_{1g} mode is attributed to the ion movement at octahedral sites. Because of the octahedral and tetrahedral oxygen vibrations, the peaks in E_g and 522 cm^{-1} in F_{2g} mode are assigned simultaneously. Two Raman peaks in the spectrum are assigned to NiO shaking peaks at approximately ~522 and 1100 cm^{-1} as a result of one (1p) and two (2p) phonon modes of two longitudinal-optical (2LO), respectively. However, as the calcination temperature rose, a peak shift of A_{1g} mode to the higher frequency region was observed due to the contribution of the nanosized effect of $NiCo_2O_4$ particles.[33,34] The exhibition of only Co-O and Ni-O vibrations confirmed the complete decomposition of their precursors. These results were consistent with XRD data.

XPS analysis was carried out to investigate further and identify the composition of the surface and the oxidation states of the species present in series NiO-$NiCo_2O_4$ microsphere catalysts with varying temperatures. Fig. S2 displays the XPS survey spectra of fresh NCO-400, NCO-500, NCO-600, and NCO-700 cathodes. As evident, the broad range spectra were enough to identify all detectable elements in all as-prepared samples, predominantly the desirable Ni 2p, Co 2p, and O 1s photoelectron lines in addition to the carbon contamination lines. Figs. 3(a, b, and c) displays the high-resolution spectrum of Ni 2p, Co 2p, and O 1s core levels of the as-synthesized NiO-$NiCo_2O_4$ samples. The peaks in Fig. 3(a) of the high-resolution Ni 2p spectrum were appropriately fitted to two spin-orbit doubles and two satellite shake-up peaks. The binding energies for nickel $2p_{3/2}$ and $2p_{1/2}$ of NCO series data accord well with the higher values presented in the literature for $NiCo_2O_4$ and are comparable to the octahedral Ni^{2+} species found in NiO.[35,36] The presence of strong satellite peaks with high spin Ni^{2+} in the oxide lattice was confirmed. The peak intensities ratio is highly reliant on the geometry and defect

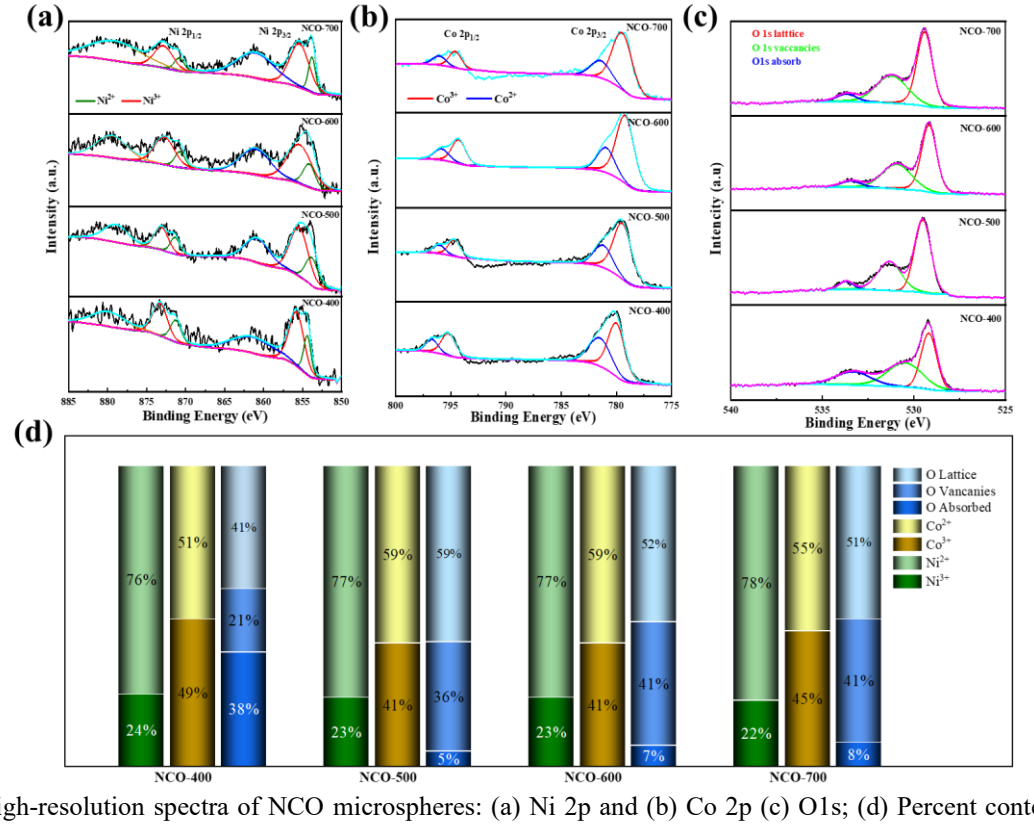

Fig. 3 The XPS high-resolution spectra of NCO microspheres: (a) Ni 2p and (b) Co 2p (c) O1s; (d) Percent content of Ni^{2+}/Ni^{3+}, Co^{2+}/Co^{3+}ions, and percent content of O 1s in NCO catalysts as designated NCO-400, NCO-500, NCO-600, NCO-700, respectively.

nature of the nickel compound, resulting from the sensitivity of the charge-transfer mechanism between the neighboring Ni^{2+} and O^{2-} orbitals. It can be noticed that the Ni^{3+} and Ni^{2+} contents of NiO-$NiCo_2O_4$ samples changed slightly following heat treatment as shown in Fig. 3(d) and all samples have almost the same Ni^{2+}/Ni^{+3} ratio of 1.3 (calculated from the corresponding peak areas). As a result, a significant portion of the nickel at the surface of NiO-$NiCo_2O_4$ is found as Ni^{2+} in octahedral positions. Fig. 3(b) shows that Co 2p can be fitted to two spin-orbit doublets and yield binding energies of ≈ 779.3 eV $2p_{3/2}$ and 794.5 eV $2p_{1/2}$ assigned to Co^{3+}, and peaks at 780.8 eV $2p_{3/2}$, 796.7 eV $2p_{1/2}$ are due to Co^{2+}. The ratio of Co^{3+}/Co^{2+} in NiO-$NiCo_2O_4$ was estimated to be 1.05 for the NCO-500, NCO-600, and NCO700. In NCO-400, a higher binding energy shift was observed, and the ratio of Co^{+3}/Co^{+2} decreased to 1.04.[35,37] These findings suggested that Ni and Co were partially oxidized and reduced in as-prepared NCO samples, respectively, for the oxygen vacancies uniformities.[38,39]

The O1s peak shape Fig. 3(c) demonstrates that the photoelectron spectrum's oxygen area, with at least three separate peak levels, has been collected by O1s lattice, O1s vacancies, and O1s absorbed.[40-42] The prominent peak, taken here to have a binding energy of around 529.3 ± 0.2 eV, for all NCO catalysts has been observed for lattice O^{2-} at approximately this value in several spinel 3d metal oxides (includes Ni-O, Co-O bonds). A second, higher-binding energy peak is found at 531.2 ± 0.1 eV and is usually regarded as the low oxygen coordinated defect sites and the surface adsorbed oxygen species. And the third peak at 533.3 ± 0.3 eV is commonly ascribed to the diversity of physic-chemisorbed water at/within the material interface.[42,43] Only a tiny percent of the overall O 1s intensity is the last peak of all samples except NCO-400 has approximately 38% of the total O 1s intensity, as shown in Fig 3(d).

As obtained in Fig. S3, The N_2 adsorption-desorption measurements have been applied at 77.3 K. All samples have mesoporous structures in type IV hysteresis loop isotherm in line with the International Union of Pure and Applied Chemistry (IUPAC) classification. The pores were generated during the pyrolysis process of nickel-cobalt precursors. The obtained isotherms of synthesized samples, BET surface area, and the structure parameters were driven and summarized in Table S2. Additionally, Barret-Joyner-Halenda (BJH) method was used to measure the pore size of the catalysts, as indicated in Fig. S3 inserted. The average pore revealed a strong peak between 2.0 nm to 50 nm, verifying the presence of mesoporous structures in NCO samples. However, a wide specific surface area can help mass transportation and increase the active sites; the electrochemically accessible surface area is more important than the physical surface area.[44] Small surface areas also may benefit from reducing side reactions resulting from less contact of the electrode with the electrolyte, in agreement with the subsequent electrochemical investigations.

The cyclic voltammograms (CV.s) measurements of the LOBs containing NCO-400, NCO-500, NCO-600, and NCO-700 microspheres were performed in aprotic 1M $LiNO_3$/DMSO electrolyte with the 0.1 mV s^{-1} scanning rate. The first cycles of the as-prepared series NCO are compared in Fig. 4(a). The NCO-600 electrode had much greater cathodic and anodic current values, as well as a wider integration area compared to the other as-prepared NCO samples, suggesting better electrocatalytic bifunctional activities towards reduction and evolution processes of the oxygen. The CV measurements of the samples NCO-500 and NCO-700 exhibited almost relative peak sizes. While in the case of the NCO-400 electrode, much lower cathodic and anodic onset potentials with a wide integration area can be obtained in comparison with the other higher calcination temperature electrodes. Galvanostatic charge/discharge tests were performed on the as-prepared NiO-$NiCo_2O_4$ heterostructure cathodes to examine their performance in aprotic Li-O_2 batteries further. Fig. 4(b) shows an excellent first complete discharge/charge capability profile for electrodes NCO-400, NCO-500, NCO-600, NCO-700, and the KB in which all the as-prepared cathodes delivered extremely high charge/discharge capacities of 20770/23163 (2.93/3.26 mAh cm^{-2}), 16250/17356 (2.29/2.45 mAh cm^{-2}), 20780/20768 (2.93/2.93 mAh cm^{-2}), 15124/15348 (2.13/2.16 mAh cm^{-2}) and 2260/2553 (0.32/0.36 mAh cm^{-2}) mAh g^{-1} with a terminal voltage window of 2.35-4.35 V vs. Li/Li^+ at 200 mAg^{-1} currents, respectively. The NCO-400 electrode exhibited a reduced charge/discharge overpotential of 0.61/0.13 V and higher charge/discharge capacity compared to the other NCO cathodes and far more significant than KB, which delivered the lower capacity and higher overpotential of 1.42/0.38 V. Fig. 4(c) displays the rate capability of NCO-400 electrodes at different current densities of 100, 200, 300, 400, and 500 mA g^{-1}. Between 2.35 and 4.35 V voltage windows. As indicated, the NCO-400 electrode delivered a higher discharge/charge capacity of 23163/18641 mAh g^{-1} (3.27/2.63 mAh cm^{-2}) at 200 mA g^{-1}current density among the other NCO electrodes (Fig. S4). At the same time, the NCO-600 electrode delivers a higher discharge/charge capacity of 19809/16641 (2.80/2.35 mAh cm^{-2}), 20089/20080 (2.83/2.83 mAh cm^{-2}), 19612/19123 (2.76/2.70 mAh cm^{-2}), and 17312/17082 (2.44/2.41 mAh cm^{-2}) mAh g^{-1} at current densities of 100, 300, 400, and 500 mA g^{-1}, respectively. The overall contribution of lithiation and pseudocapacitive charge storage to the overall discharge capacity can be negligible under a super high working potential of 2.35-4.35 V, especially when the discharge capacity of this contribution is over 20 times higher than these reported Li-ion batteries. This phenomenon was previously demonstrated in many comparable papers when operating the battery in an inert gas circumstance.[17,42,43] The cycle stability of lithium-oxygen batteries with different electrodes and KB was tested under different current densities by a fixed specific capacity method.

Figure 4(d) contains the end voltage of each cycle and the

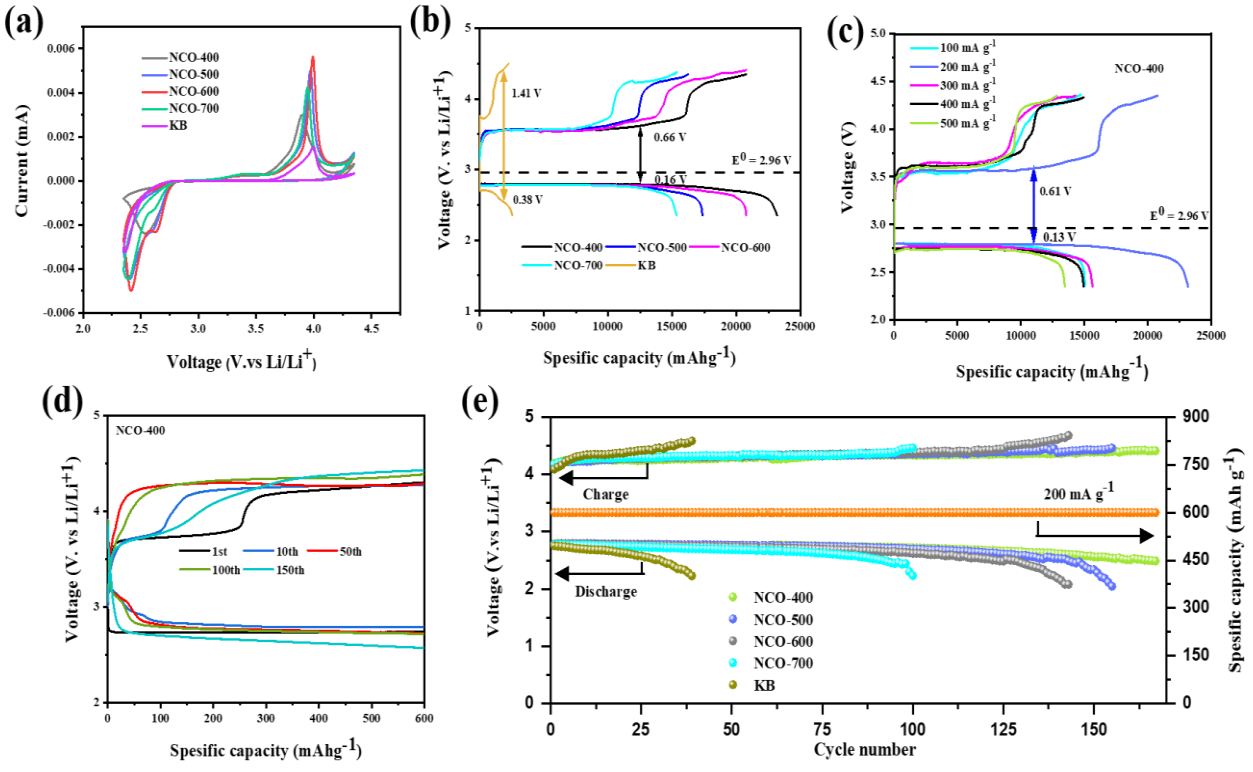

Fig. 4 (a) Cyclic voltammetry curves (CV) of the first cycles of fresh NCO series electrodes at a scan rate of 0.1 mV s^{-1} within a voltage window of 2.35-4.35 V; (b) Specific capacity of Li-O_2 batteries with a series of as-prepared NCO catalysts at a current density of 200 mA g^{-1}; (c) Rate capability of NCO-400 electrode utilizing different current densities and cutoff voltage of 2.35-4.35 V; (d) The cycling performance of NCO-400 electrode at a current density of 200 mA g^{-1} at a fixed capacity of 600 mAh g^{-1} and (e) the terminal discharge/charge voltages of the NCO electrodes at a current density of 200 mA g^{-1} at a fixed specific capacity of 600 mAh g^{-1}.

corresponding cycle discharge/charge curve. When the capacity is fixed at 600 mAh g^{-1}, among the four NCO electrodes, the battery using NCO-400 as the positive electrode material can be continuously cycled for 170 cycles at a current density of 200 mA g^{-1}. It can be operated at a voltage of 2.6 V during the first 140 cycles. They keep a stable charge/discharge platform where the lithium intercalation reaction has a negligible effect on the electrode's discharge capability. When the capacity limitation increases to 1000 mAh g^{-1}, the NCO-400 electrode also displayed better cyclability than the other electrodes. It can work stably for 90 cycles, and it shows a stable discharge/charge platform during the cycling, as displayed in Fig. S5. In contrast to a number of the sample NiO-based and $NiCO_2O_4$-base electrodes described in the literature, Table 1 summed the battery performance comparisons with the obtained heterostructure NCO-400 electrode in this work. It was clearly shown that under comparable test circumstances of capacity and durability, the electrode NCO-400 showed a higher performance than most other electrodes, making it a viable material for improved Li-O_2 batteries. The combination of $NiCo_2O_4$ with NiO plays a significant role in an exhibition of an improvement in the catalytic activity of the Li-O_2 batteries, where $NiCo_2O_4$ aids both ORR and OER processes. In addition, the distinctive necklace-like heterostructure microspheres offer benefits. The particular shape enables continuous oxygen flow, and the heterostructure encourages lithium ions and electrons movement, which further improves battery performance.

NCO-400 cathode electrode was picked up as it showed higher capacity and cycle performance among the other electrodes to comprehend the kinetics and reaction mechanism involved in the ORR/OER process. To investigate and better understand the excellent capacity retention and charge transportations mechanism on the surface of the electrodes, the electrochemical impedance spectroscopy (EIS) technique was performed on different catalysts before and after the cyclic voltammetry measurement at open-circuit potential with 10^5 to 0.01 Hz frequency range. As demonstrated in Fig. 5(a), the semicircles shown in the high-frequency range are related to the resistance of the charge transferring. The slope line at the low-frequency range can be referred to as the ion diffusion process within the electrode.[45,46] A slight increase in the charge transfer resistance values was observed after cyclic voltammetry tests contributed from the insulating discharge products formed and partially decomposed as indicated in Fig. S6. All as-prepared NCO series electrodes showed lower charge transfer resistance, implying their excellent electrocatalytic activity and fasting the kinetics critical for Li-O_2 batteries. For further investigation on charge/discharge

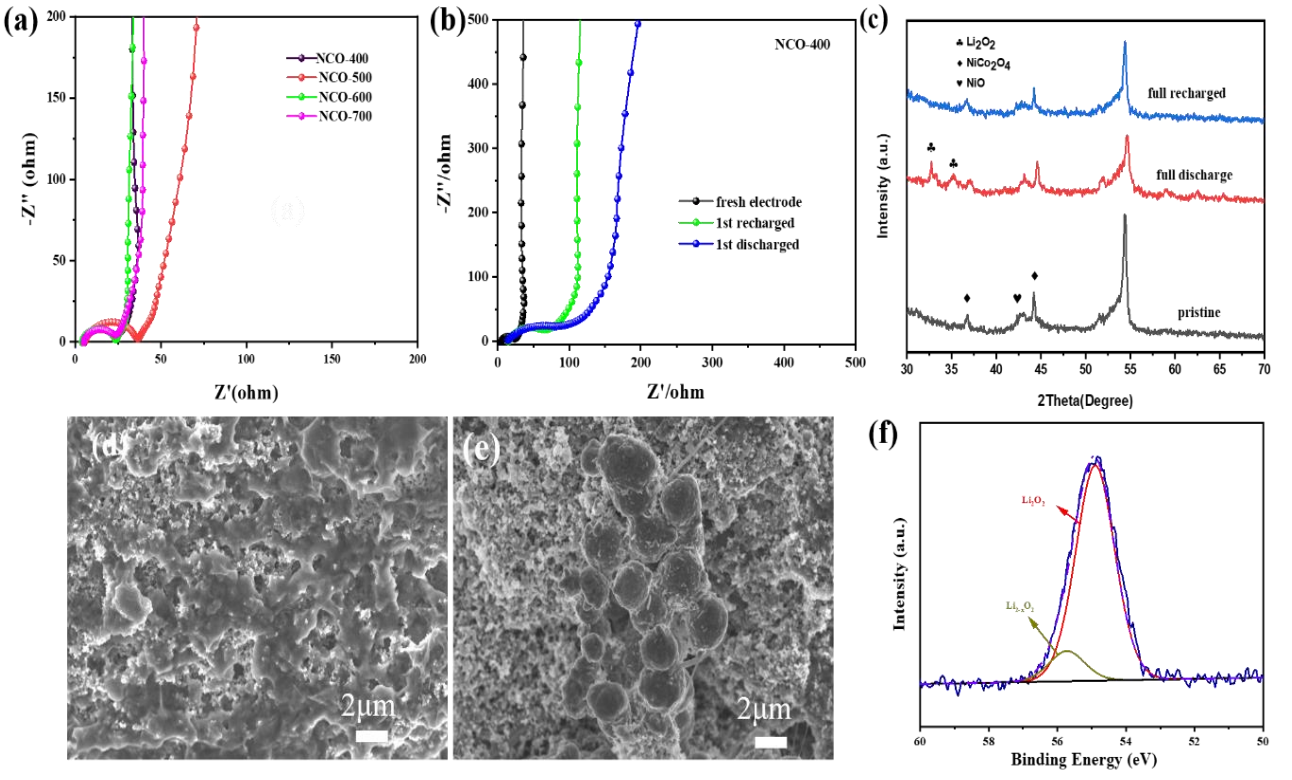

Fig. 5 (a) Electrochemical impedance spectra of NCO-400, NCO-500, NCO-600, and NCO-700 fresh electrodes; (b) EIS plots of the NCO-400 cathode at different states; (c) The XRD pattern of the NCO-400 before and after discharge, and after recharged; SEM image of NCO-400 electrode at (d) the 1st cycle discharged to 2.35 V and (e), the 1st cycle recharged to 4.35; (f) The XPS of Li 1s spectra after the first cycle when discharged at the current density of 200 mA g^{-1} and capacity limit of 1000 mAh g^{-1}.

Table 1. The performance of the NCO-400 cathode in Li-O_2 batteries compared to that of NiO-based and $NiCo_2O_4$-based cathodes described in the literature.

Cathode materials	Morphologies	Full discharge capacity mAh g^{-1}/current density mA g^{-1}	Cycles/fixed capacity mAh g^{-1}/current density mA g^{-1}
RuO_2/NiO [47]	Nanosheets	3240/250	50/500/250
NiO-$NiCo_2O_4$[48]	Urchin-like	9231/100	80/600/100
$NiCo_2O_4$ /Ni foam [49]	Nanosheets	7004/40	100/500/100
NiO [50]	Nanosheets	1260/100	40/500100
$NiCo_2O_4$[51]	Flower-like	3163/0.08 mA cm^{-2}	60/500/0.08 mA cm^{-2}
$NiCo_2O_4$[52]	Nanoflakes	1560 / 0.2 mA cm^{-2}	50/300/0.2 mA cm^{-2}
NCO@NCF [53]	Nanofibers	5304/200	92/1000/200
$NiCo_2O_4$@Co_3O_4[54]	Nanorods	4386/ 0.1 mA cm^{-2}	60/500/ 0.1 mA cm^{-2}
NCO@GF [55]	Needell-like	5000/400	80/1000/400
NiO-$NiCo_2O_4$ (This work)	Rod-like	23163/200	170/600/200

characteristics, the electrochemical impedance test was also applied on the NCO-400 electrode. As shown in Fig. 5(b), after the first discharge cycle, an increase in semicircle diameter was observed compared to the fresh electrode; due to the formation of discharge product Li_2O_2 on the surface of the cathode, which hypothetically, hinders and resists the electrons transferring leading to high electrical resistance. On charging, the Li_2O_2 decomposed; as a result, the charge transferee resistance was reduced compared to the fresh electrode. Thus, it suggested the reversibility of discharge product production and degradation. As the electrode goes deeper in cycles, the electrolyte decomposes, and more by-products form, hence struggling with electron transfer.[48] Ex-situ XRD examinations were carried out to better understand the changes in the electrode composition during the complete discharge/recharge stages. Fig. 5(c) displayed the NCO-400 pristine electrode, after discharge to 2.35 V and recharge to 4.35 V. Following the first complete discharge of 2.35 V, distinctive Li_2O_2 peaks develop on the electrode compared to the fresh electrode's XRD pattern. These two peaks were ascribed to (100) and (101) Li_2O_2, showing that Li_2O_2 is the most prevalent crystalline discharge product.[56,57] The peaks of

Li_2O_2 were not seen in the XRD pattern after being recharged to 4.35 V. The results show that the NCO-400 electrode has excellent catalytic properties toward the Li_2O_2's production and decomposition efficiently. SEM was used to evaluate the shape of the discharge product. Figs. 5(d-e) display the NCO-400 microsphere scanned image. After fully discharging the cell to 2.35 V, the necklace-like spheres were enveloped in a Li_2O_2 film, as presented in Fig. 5(d). After recharging to 4.35 V in Fig. 5(e), NCO spheres can be reobserved, which means that the film Li_2O_2 products can be fully decomposed in the favor of catalytic NCO. Generally, the morphology of Li_2O_2 depends on the solubility of LiO_2, whether it is produced as particles or films.[58-60] The high solvent LiO_2 mechanism produced a particulate-like Li_2O_2, whereas the film-like Li_2O_2 is produced by a low soluble LiO_2 surface growth model. In our situation, film-like Li_2O_2 has been generated on the necklace-like NiO-$NiCo_2O_4$ microspheres cathode via a surface growth pathway, resulting in a comprehensive interface between the discharge product and the positive electrode surfaces.[61,62] As a result, electron transmission during the charging process was made more accessible, resulting in less charge overpotential. The ex-situ high-resolution XPS from Li 1s was performed after the first cycle when discharged at the current density of 200 mA g^{-1} and capacity limit of 1000 mAh g^{-1}. The Li_2O_2 discharge product can be linked with binding energy in Li 1s profiles at about 54.9 eV. In comparison, $Li_{2-x}O_2$, a combination of LiO_2 and Li_2O_2, is responsible for the binding energy at 55.8 eV.[48] The release products were largely Li_2O_2; the peaks of $Li_{2-x}O_2$ were also identified in minor intensities indicating that undecomposed release products were available.

4. Conclusion

As discussed in the introduction, the Li-O_2 battery can be the "holy grail" of electrochemical energy storage technologies. However, many challenges and problems need to be solved for it to be a commercially viable technology. Improving the air cathode electrocatalytic activity can significantly enhance the performance of the battery. This work has outlined a significant effort to create new electrocatalytic cathodes for improving the Li-O_2 battery performance. Necklace-like heterostructure NiO-$NiCo_2O_4$ microsphere was effectively synthesized using a simple hydrothermal-assisted technique. The as-prepared electrodes exhibited considerable specific capacities and favorable cyclic performance. At a current density of 200 mA g^{-1}, the constructed batteries with NCO-400 as a catalyst achieved a significant discharge/charge capacity of 23163/20770 mAh g^{-1}. Moreover, the NCO-400 displayed a decreased overpotential, good rate capability, and cycling stability and cycled more than 170 times at 200 mA g^{-1} under 600 mAh g^{-1}. The unusual combination of NiO-$NiCo_2O_4$ resulted in this higher electrocatalytic activity. Furthermore, the unique morphology can supply adequate reaction sites for Li_2O_2 deposition and breakdown, while allowing continuous oxygen flow and charge transport throughout the cycle. As results showed, the introduction of the NiO-$NiCo_2O_4$ heterostructure microsphere appears to be potential cathode catalyst material for Li-O_2 batteries.

Acknowledgments

This work was supported by the National Key R&D Program of China of 2017YFE0195200 and 2018YFE0103500, the Open Program of the State Key Laboratory of Marine Resource Utilization in the South China Sea.

Conflict of interest

There are no conflicts to declare.

Supporting information

Applicable.

References

[1] G. Girishkumar, B. McCloskey, A. C. Luntz, S. Swanson, W. Wilcke, *The Journal of Physical Chemistry Letters*, 2010, **1**, 2193-2203, doi: 10.1021/jz1005384.

[2] D. Capsoni, M. Bini, S. Ferrari, E. Quartarone, P. Mustarelli, *Journal of Power Sources*, 2012, **220**, 253-263, doi: 10.1016/j.jpowsour.2012.07.123.

[3] A. Kraytsberg, Y. Ein-Eli, *Journal of Power Sources*, 2011, **196**, 886-893, doi: 10.1016/j.jpowsour.2010.09.031.

[4] R. Padbury, X. Zhang, *Journal of Power Sources*, 2011, **196**, 4436-4444, doi: 10.1016/j.jpowsour.2011.01.032.

[5] P. G. Bruce, S. A. Freunberger, L. J. Hardwick, J. M. Tarascon, *Nature Materials*, 2012, **11**, 19-29, doi: 10.1038/nmat3191.

[6] J. Hassoun, H. G. Jung, D. J. Lee, J. B. Park, K. Amine, Y. K. Sun, B. Scrosati, *Nano Letters*, 2012, **12**, 5775-5779, doi: 10.1021/nl303087j.

[7] F. Wu, Y. Xing, L. Li, J. Qian, W. Qu, J. Wen, D. Miller, Y. Ye, R. Chen, K. Amine, J. Lu, *ACS Applied Materials & Interfaces*, 2016, **8**, 23635-23645, doi: 10.1021/acsami.6b05403.

[8] E. Frackowiak, F. Béguin, *Carbon*, 2001, **39**, 937-950, doi: 10.1016/s0008-6223(00)00183-4.

[9] N. Ding, S. W. Chien, T. S. A. Hor, R. Lum, Y. Zong, Z. Liu, *Journal of Materials Chemistry A*, 2014, **2**, 12433-12441, doi: 10.1039/c4ta01745e.

[10] S. Ma, Y. Wu, J. Wang, Y. Zhang, Y. Zhang, X. Yan, Y. Wei, P. Liu, J. Wang, K Jiang, *Nano Letters*, 2015, **15**, 8084-8090, doi: 10.1021/acs.nanolett.5b03510.

[11] J. J. Xu, Z. L. Wang, D. Xu, L. L. Zhang, X. B. Zhang, *Nature Communications*, 2013, **4**, 2438, doi: 10.1038/ncomms3438.

[12] T. V. Pham, H. P. Guo, W. B. Luo, S. L. Chou, J. Z. Wang, H. K. Liu, *Journal of Materials Chemistry A*, 2017, **5**, 5283-5289, doi: 10.1039/c6ta10751f.

[13] D. Sun, Y. Shen, W. Zhang, L. Yu, Z. Yi, W. Yin, D. Wang, Y. Huang, J. Wang, D. Wang, J. B. Goodenough, *Journal of the American Chemical Society*, 2014, **136**, 8941-8946, doi: 10.1021/ja501877e.

[14] H. D. Lim, H. Song, J. Kim, H. Gwon, Y. Bae, K. Y. Park, J. Hong, H. Kim, T. Kim, Y. H. Kim, X. Lepró, R. Ovalle-Robles, R. H. Baughman, K. Kang, *Angewandte Chemie International*

Edition, 2014, **53**, 3926-3931, doi: 10.1002/anie.201400711.
[15] D. J. Lee, H. Lee, Y. J. Kim, J. K. Park, H. T. Kim, *Advanced Materials*, 2016, **28**, 857-863, doi: 10.1002/adma.201503169.
[16] J. I. Jung, H. Y. Jeong, M. G. Kim, G. Nam, J. Park, J. Cho, *Advanced Materials*, 2015, **27**, 266-271, doi: 10.1002/adma.201403897.
[17] B. He, J. Wang, J. Liu, Y. Li, Q. Huang, Y. Hou, G. Li, J. Li, R. Zhang, J. Zhou, W. Tian, Y. Du, F. Dang, H. Wang, B. Kong, *Advanced Energy Materials*, 2020, **10**, 1904262, doi: 10.1002/aenm.201904262.
[18] M. Hong, H. C. Choi, H. R. Byon, *Chemistry of Materials*, 2015, **27**, 2234-2241, doi: 10.1021/acs.chemmater.5b00488.
[19] Y. Jiang, J. Cheng, L. Zou, X. Li, Y. Gong, B. Chi, J. Pu, J. Li, *Electrochimica Acta*, 2016, **210**, 712-719, doi: 10.1016/j.electacta.2016.05.199.
[20] J. Zhou, Y. Huang, X. Cao, B. Ouyang, W. Sun, C. Tan, Y. Zhang, Q. Ma, S. Liang, Q. Yan, H. Zhang, *Nanoscale*, 2015, **7**, 7035-7039, doi: 10.1039/c4nr06527a.
[21] Z. Jian, P. Liu, F. Li, P. He, X. Guo, M. Chen, H. Zhou, *Angewandte Chemie International Edition*, 2014, **53**, 442-446, doi: 10.1002/anie.201307976.
[22] Z. Guo, G. Zhu, Z. Qiu, Y. Wang, Y. Xia, *Electrochemistry Communications*, 2012, **25**, 26-29, doi: 10.1016/j.elecom.2012.09.022.
[23] Z. D. Yang, Z. W. Chang, J. J. Xu, X. Y. Yang, X. B. Zhang, *Science China Chemistry*, 2017, **60**, 1540-1545, doi: 10.1007/s11426-017-9156-0.
[24] H. Dong, P. Tang, X. Wang, K. Li, Y. Wang, D. Wang, H. Liu, S. Yang, C. Wu, *ACS Applied Materials & Interfaces*, 2019, **11**, 39789-39797, doi: 10.1021/acsami.9b11623.
[25] S. V. Devaguptapu, S. Hwang, S. Karakalos, S. Zhao, S. Gupta, D. Su, H. Xu, G. Wu, *ACS Applied Materials & Interfaces*, 2017, **9**, 44567-44578, doi: 10.1021/acsami.7b16389.
[26] Z. Qin, Q. Cheng, Y. Lu, J. Li, *Applied Physics A*, 2017, **123**, 492, doi: 10.1007/s00339-017-1108-x.
[27] J. F. Marco, J. R. Gancedo, M. Gracia, J. L. Gautier, E. Ríos, F. J. Berry, *Journal of Solid-State Chemistry*, 2000, **153**, 74-81, doi: 10.1006/jssc.2000.8749.
[28] H. P. Klug, L. E. Alexander, X-ray diffraction procedures: for polycrystalline and amorphous materials, 2nd edition, 1974.
[29] Y. Q. Wu, X. Y. Chen, P. T. Ji, Q. Q. Zhou, *Electrochimica Acta*, 2011, **56**, 7517-7522, doi: 10.1016/j.electacta.2011.06.101.
[30] S. Verma, H. M. Joshi, T. Jagadale, A. Chawla, R. Chandra, S. Ogale, *The Journal of Physical Chemistry C*, 2008, **112**, 15106-15112, doi: 10.1021/jp804923t.
[31] M. Cabo, E. Pellicer, E. Rossinyol, O. Castell, S. Suriñach, M. Dolors Baró, *Crystal Growth & Design*, 2009, **9**, 4814-4821, doi: 10.1021/cg900648q.
[32] E. Umeshbabu, G. Rajeshkhanna, P. Justin, G. R. Rao, *Materials Chemistry and Physics*, 2015, **165**, 235-244, doi: 10.1016/j.matchemphys.2015.09.023.
[33] N. Mironova-Ulmane, A. Kuzmin, I. Sildos, M. Pärs, *Open Physics*, 2011, **9**, 1096-1099, doi: 10.2478/s11534-010-0130-9.
[34] Y. Huang, W. Fan, B. Long, H. Li, W. Qiu, F. Zhao, Y. Tong, H. Ji, *Journal of Materials Chemistry A*, 2016, **4**, 3648-3654, doi: 10.1039/c5ta09370h.
[35] Q. Tang, M. Chen, L. Wang, G. Wang, *Journal of Power Sources*, 2015, **273**, 654-662, doi: 10.1016/j.jpowsour.2014.09.139.
[36] C. Mahala, M. Basu, *ACS Omega*, 2017, **2**, 7559-7567, doi: 10.1021/acsomega.7b00957.
[37] J. F. Marco, J. R. Gancedo, M. Gracia, J. L. Gautier, E. I. Ríos, H. M. Palmer, C. Greaves, F. J. Berry, *Journal of Materials Chemistry*, 2001, **11**, 3087-3093, doi: 10.1039/b103135j.
[38] D. Liu, C. Zhang, Y. Yu, Y. Shi, Y. Yu, Z. Niu, B. Zhang, *Nano Research*, 2018, **11**, 603-613, doi: 10.1007/s12274-017-1670-8.
[39] C. Chang, L. Zhang, C. W. Hsu, X. F. Chuah, S. Y. Lu, *ACS Applied Materials & Interfaces*, 2018, **10**, 417-426, doi: 10.1021/acsami.7b13127.
[40] L. Liu, H. Zhang, L. Fang, Y. Mu, Y. Wang, *Journal of Power Sources*, 2016, **327**, 135-144, doi: 10.1016/j.jpowsour.2016.07.054.
[41] Y. Lei, Y. Wang, W. Yang, H. Yuan, D. Xiao, *RSC Advances*, 2015, **5**, 7575-7583, doi: 10.1039/c4ra15097j.
[42] L. Liu, J. Wang, Y. Hou, J. Chen, H.-K. Liu, J. Wang, Y. Wu, *Small*, 2016, **12**, 602-611, doi: 10.1002/smll.201502924.
[43] C. An, Y. Wang, Y. Huang, Y. Xu, L. Jiao, H. Yuan, *Nano Energy*, 2014, **10**, 125-134, doi: 10.1016/j.nanoen.2014.09.015.
[44] S. R. Narayan, A. Manohar, S. Mukerjee, *The Electrochemical Society Interface*, 2015, **24**, 65.
[45] J. Zhang, F. Liu, J. P. Cheng, X. B. Zhang, *ACS Applied Materials & Interfaces*, 2015, **7**, 17630-17640, doi: 10.1021/acsami.5b04463.
[46] E. Jokar, A. I. Zad, S. Shahrokhian, *Journal of Solid State Electrochemistry*, 2015, **19**, 269-274, doi: 10.1007/s10008-014-2592-y.
[47] P. Tan, Z. H. Wei, W. Shyy, T. S. Zhao, X. B. Zhu, *Energy & Environmental Science*, 2016, **9**, 1783-1793, doi: 10.1039/c6ee00550k.
[48] W. Zhao, X. Li, R. Yin, L. Qian, X. Huang, H. Liu, J. Zhang, J. Wang, T. Ding, Z. Guo, *Nanoscale*, 2019, **11**, 50-59, doi: 10.1039/c8nr08457b.
[49] C. Shen, Z. Wen, F. Wang, K. Rui, Y. Lu, X. Wu, *Journal of Power Sources*, 2015, **294**, 593-601, doi: 10.1016/j.jpowsour.2015.06.130.
[50] S. Tong, M. Zheng, Y. Lu, Z. Lin, J. Li, X. Zhang, Y. Shi, P. He, H. Zhou, *Journal of Materials Chemistry A*, 2015, **3**, 16177-16182, doi: 10.1039/c5ta03685b.
[51] L. Wang, T. Zhu, Z. Lyu, J. Zhang, L. Gong, S. Xiao, J. Liu, W. Dong, X. Cui, G. W. Ho, W. Chen, *RSC Advances*, 2016, **6**, 98867-98873, doi: 10.1039/c6ra21414b.
[52] L. Zhang, S. Zhang, K. Zhang, G. Xu, X. He, S. Dong, Z. Liu, C. Huang, L. Gu, G. Cui, *Chemical Communications*, 2013, **49**, 3540, doi: 10.1039/c3cc40393a.
[53] H. Xue, X. Mu, J. Tang, X. Fan, H. Gong, T. Wang, J. He, Y. Yamauchi, *Journal of Materials Chemistry A*, 2016, **4**, 9106-9112, doi: 10.1039/C6TA01712F.
[54] P. Sennu, H. S. Park, K. U. Park, V. Aravindan, K. S. Nahm, Y.-S. Lee, Journal of Catalysis, 2017, **349**, 175-182, doi:

10.1016/j.jcat.2017.03.015.
[55] Y. Jiang, L. Zou, J. Cheng, Y. Huang, L. Jia, B. Chi, J. Pu, J. Li, ChemElectroChem, 2017, **4**, 3140-3147, doi: 10.1002/celc.201700864.
[56] L. Liu, J. Wang, Y. Hou, J. Chen, H. K. Liu, J. Wang, Y. Wu, *Small*, 2016, **12**, 602-611, doi: 10.1002/smll.201502924.
[57] Z. Jian, P. Liu, F. Li, P. He, X. Guo, M. Chen, H. Zhou, *Angewandte Chemie International Edition*, 2014, **53**, 442-446, doi: 10.1002/anie.201307976.
[58] J. L. Shui, J. S. Okasinski, P. Kenesei, H. A. Dobbs, D. Zhao, J. D. Almer, D. J. Liu, *Nature Communications*, 2013, **4**, 2255, doi: 10.1038/ncomms3255.
[59] Y. Wang, Y. C. Lu, *Energy Storage Materials*, 2020, **28**, 235-246, doi: 10.1016/j.ensm.2020.03.007.
[60] Z. Sadighi, J. Liu, F. Ciucci, J. K. Kim, *Nanoscale*, 2018, **10**, 15588-15599, doi: 10.1039/c8nr03942a.
[61] X. Ren, M. Huang, S. Luo, Y. Li, L. Deng, H. Mi, L. Sun, P. Zhang, *Journal of Materials Chemistry A*, 2018, **6**, 10856-10867, doi: 10.1039/C8TA03345E.
[62] Y. Xing, Y. Yang, R. Chen, M. Luo, N. Chen, Y. Ye, J. Qian, L. Li, F. Wu, S. Guo, *Small*, 2018, **14**, 1704366, doi: 10.1002/smll.201704366.

Author Information

Zeinab Mohamed *is a Ph.D. candidate in Material Science at the School of Material Science and Engineering of the University of Science and Technology of China in Hefei, China. She earned an M.Sc. in Chemistry from Sudan University of Science and Technology in 2015, as well as an MSc. in Material Science and Engineering from Shandong University in Jinan, China, In the year 2021. In 2019, she was granted the Chinese Government's Outstanding International Student Scholarship. She worked as a lecturer at Sudan's University of Medical Science and Technology's Department of Chemistry from 2016 to 2018. Her research interest areas include Electrochemical Energy Conversion and Storage Technologies.*

Guoliang Zhang *is currently a Ph.D. candidate in the Key Laboratory for Liquid-Solid Structural Evolution and Processing of Materials at Shandong University. He received his bachelor's degree in 2015 in School of Material Science and Engineering from Shandong University of Science and Technology. His current research is focused on designing cathode catalysts for Lithium-oxygen batteries.*

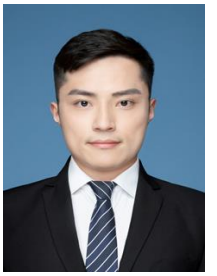

Biao He *is currently a Ph.D. student, and working as research assistant as well at the Institute for Materials, Faculty of Mechanical Engineering of Ruhr-Universität Bochum. He obtained a master's degree in Materials Engineering with the Principle Prize for best graduate student in Shandong University, and the outstanding thesis of Shandong Province in 2020. His research interests include studying of Catalyst Materials, Clean and Sustainable Energy Technologies, and Electrochemical Energy Conversion and Storage systems.*

Yuqi Fan *received her M.S. and Ph.D. degrees from Graduate School of Life and Environmental Sciences, University of Tsukuba, Japan, in 2014 and 2017, respectively. She then joined Shandong Normal University, China, in 2017, and now she is a Lecturer in the Institute of Environment and Ecology. Her research interests include studying of Integrative Environment and Biomass Sciences, Sustainable Energy Technologies, and Catalyst Materials for Energy storage and Conversion.*